Materials and Design 198 (2021) 109366

Contents lists available at ScienceDirect

Materials and Design

journal homepage: www.elsevier.com/locate/matdes

A sub-500 mV monolayer hexagonal boron nitride based memory device

Jun Ge [a,b,*,1], Haiming Huang [a,b,1], Zelin Ma [b], Weilong Chen [b], Xucheng Cao [b], Huaheng Fang [b], Jianfeng Yan [b], Zhiyu Liu [a,b], Weiliang Wang [c], Shusheng Pan [a,b,*]

[a] Research Center for Advanced Information Materials (CAIM), Huangpu Research and Graduate School of Guangzhou University, Guangzhou 510006, China
[b] Solid State Physics & Material Research Laboratory, School of Physics and Material Science, Guangzhou University, Guangzhou 510006, China
[c] State Key Laboratory of Optoelectronic Materials and Technologies, School of Physics, Guangdong Province Key Laboratory of Display Material and Technology, Sun Yat-sen University, Guangzhou 510275, China

HIGHLIGHTS

- Memristive device based on monolayer hexagonal boron nitride is demonstrated.
- An interfacial polymer layer is inserted to constrain the conducting filament size and numbers.
- The device shows low operating voltage (< 500 mV), large on/off ratio, long retention time, and excellent flexibility.
- Tunneling conduction is shown in off-state and on-state current conducts via metallic conducting filaments.

GRAPHICAL ABSTRACT

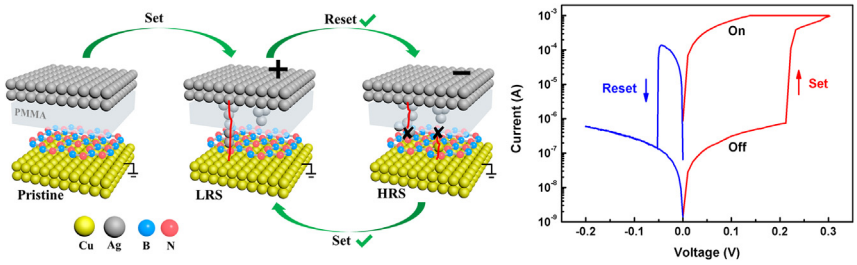

ARTICLE INFO

Article history:
Received 6 October 2020
Received in revised form 24 November 2020
Accepted 25 November 2020
Available online 28 November 2020

Keywords:
Nonvolatile memory
Boron nitride
Resistive switching
Monolayer
Low operating voltage

ABSTRACT

The recent discovery of memristive devices based on two-dimensional materials have attracted much interest for emerging applications on flexible memory, neuromorphic computing, and so forth. Reducing the thickness to a single-layer level would prompt the scaling limit to sub-nanometer. However, monolayer materials based vertical memristive devices generally suffer inferior performance with high operating voltage, large leakage currents, and poor reliability. In this study, an interfacial polymer layer is inserted between the monolayer hexagonal boron nitride (h-BN) and top electrodes, which not only helps to constrain the conducting filament size but also block the formation of excess filaments from the bottom Cu foil. Therefore, the device shows stable bipolar resistive switching behavior with low operating voltage (< 500 mV), large on/off ratio (up to 10^5), long retention time (> 10^5 s), and excellent flexibility. It is demonstrated that tunneling conduction is shown in off-state and on-state current conducts via metallic conducting filaments, which are formed by the substitute of metal ions for lattice vacancies in h-BN. This work presents a scalable interface engineering strategy to control the interactions between metal ions and defects in monolayer h-BN films and sheds light on their promising application for large-scale integrated ultrathin flexible memory.

© 2020 The Author(s). Published by Elsevier Ltd. This is an open access article under the CC BY license (http://creativecommons.org/licenses/by/4.0/).

1. Introduction

Two-dimensional (2D) materials have triggered great interest for advanced electronic devices over the past decades owing to their ultimately atomic thickness, a wide range of bandgaps, high mechanical flexibility, etc. [1–12] Among these technologies, the resistive random access memory (RRAM), in which the resistance state can be switched

* Corresponding authors.
E-mail addresses: speegejun510@gzhu.edu.cn (J. Ge), sspan@gzhu.edu.cn (S. Pan).
[1] These authors contributed equally to this work.

https://doi.org/10.1016/j.matdes.2020.109366
0264-1275/© 2020 The Author(s). Published by Elsevier Ltd. This is an open access article under the CC BY license (http://creativecommons.org/licenses/by/4.0/).

between at least two states by an external electrical stimulus, have been extensively explored for various applications such as digital memories, neuromorphic platforms, and bio-inspired sensing system [13–19]. In this regard, ultrathin 2D nanomaterials, such as graphene and transition metal dichalcogenide, including MoS_2, WS_2, TiS_2, TaS_2, etc., have raised increasing attention for RRAM during the past few years, due to their unique 2D morphology and ultrathin thickness [14]. For example, several solution-processed 2D-MoS_2 nanobelts based devices have successfully demonstrated resistive memory effect with a high ON/OFF ratio up to ~10^4 and long retention time (> 10^4 s) [20,21]. Monolayer MoS_2 devices with a lateral structure have also been investigated, where the memristive behavior is attributed to the migration of anions together with the presence of grain boundaries [22–24].

To reduce the footprint and increase the scaling capability, vertical devices with atomic-thickness are preferable. In this regard, few-layer transition metal dichalcogenides (MX_2, M = Mo, W; X = S, Se) and hexagonal boron nitride (h-BN) sandwiched vertically between metal electrodes have been studied and exhibited reproducible bipolar or unipolar resistive switching [25–28]. It is of great scientific importance to further decrease the thickness of 2D materials to the level of monolayer while retaining the resistive switching functionality. The ultrathin active layer can potentially offer more desirable device properties such as low working voltage, ultra-dense integration, and high-speed switching. More importantly, realizing the memristive effect at the atomic level might lead to new switching mechanisms and thus novel device concepts. Akinwande et al. pioneered to study the resistance switching phenomenon in a variety of single-layer atomic sheets and demonstrated relatively promising properties, such as large on/off ratio (up to 10^7) and fast switching speed (<15 ns) [29–31]. However, those devices generally require transfer and lithography process, with relatively low device yield (~50%) and large switching voltage (2–3 V), which might come from the chemical residues due to the complex fabrication process. Furthermore, the transfer techniques are not applicable for achieving large-scale integrated device arrays. The lithography and transfer-free devices have also been reported; however, the device properties are degraded with a smaller on/off ratio ($\langle 10^2$) due to the large leakage current [31,32] and the reliability of the device is still in a debate [14,33].

In this work, a transfer and lithography-free resistive switching device based on chemical vapor deposition (CVD) grown monolayer hexagonal boron nitride (h-BN) vertically sandwiched by different metallic electrodes was reported. h-BN is a typical 2D insulator material, with large band gap and outstanding thermal characteristics, making it a promising candidate for resistive switching applications [27,34,35]. An interfacial polymer layer is designed to insert between the h-BN and top electrodes. Such devices show bipolar nonvolatile switching with low operating voltage, large on/off ratio, long retention time, and excellent flexibility. The conductive atomic force microscopy, temperature-dependent electron transport studies, and ab-initio simulations have proven that the substitute of metal ions for lattice vacancies results in filamentary conducting channels during the resistance switches. Importantly, the inserting polymer layer help to constrain the conducting filament size and block the formation of unwanted filament from the bottom electrode, and thus facilitating to obtain the monolayer h-BN resistive memory device with improved performance.

2. Experimental section

Fabrication of Memory Device: The large-area CVD-grown monolayer h-BN was purchased from 6Carbon Technology. A solution of PMMA in toluene (5 mg mL^{-1}) was deposited on the h-BN film by spin-coating at 3000 rpm for 30 s. To complete the device fabrication, top electrodes with a radius of 50 um were deposited on the PMMA/δ-phase $CsPbI_3$ by direct thermal evaporation using a shadow mask.

Material and Device Characterization: The XPS (ThermoFisher, Nexsa with monochromatic Al Kα X-ray), SEM (FEI, Quanta 650) AFM (Bruker, Dimension Edge) were employed to characterize the as-grown samples. The current—voltage (I — V) curves were obtained by using a Keithley B2902A with a two-probe configuration. The growth substrate, Cu foil, served as the global bottom electrode, which was electrically grounded, and an external bias was applied to the top electrode.

Computational Methods: The structural and electronic properties were evaluated with spin-polarized density functional theory (DFT) based on the pseudopotential plane-wave method. The Vienna ab initio simulation package (VASP) was applied for building optimization system and electronic analysis. Generalized gradient approximation (GGA) in the Perdew–Burke–Ernzerhof (PBE) form was chosen as exchange-correlation energy. The kinetic energy cutoff was 400 eV. In order to eliminate interactions between adjacent images, 12 Å of vacuum separation along the direction normal to the basal plane was used. All atoms are fully relaxed until the force on each atom is less than 0.01 eV/Å. An equivalent Monkhorst–Pack k grid of $5 \times 5 \times 1$ ($25 \times 25 \times 1$) is used for doped BN where 4% boron atoms are replaced by doped atoms in structural relaxation (static calculations). Gaussian smearing of 0.14 eV was used.

3. Results and discussion

The large-area CVD-grown monolayer h-BN was purchased from a commercial company. Cu foil was chosen as the substrate owing to its excellent compatibility for h-BN growth and relatively low cost. The film stoichiometry is confirmed by x-ray photoelectron spectroscopy (XPS), as shown in Fig. 1a and b. The calculated ratio of B and N atoms is 1.03:1 (see Fig. S1 for details) and the inset in Fig. 1a indicates a negligible CuO peak (the Cu^{2+} satellite peak near 943 eV) in Cu 2p core-level spectra. The influence on resistive switching (RS) behaviors of the small amount of CuO, which might locate at the film/bottom electrode (BE) interface, will be discussed in the subsequent text. Fig. 1c shows the SEM image of h-BN on Cu foil. The film growth is fully complete and an open Cu surface can hardly be found. Besides, sites with multiple layers, marked by the red triangles (a zoomed-in image is shown in the inset of Fig. 1c), also appear. The presence of the multilayer sites is consistent with previous reports on the synthesis of monolayer h-BN on Cu foil using the CVD method, suggesting the growth of h-BN on Cu is not self-limited [36]. To confirm the monolayer nature of the background layer of h-BN, the film is transferred onto a SiO_2/Si substrate and atomic force microscopy (AFM) was conducted to examine the film thickness. It is worth noting that the as-transferred sample has been annealed under the H_2 atmosphere before the AFM measurement to eliminate the gap between the h-BN and the substrate and remove the chemical residues due to the transfer process. The typical thickness of h-BN is less than 0.486 nm, in accordance with the monolayer growth (the theoretical value of the c-axis spacing for h-BN is ~0.33 nm).

The RS properties of Ag/h-BN/Cu structure devices was first measured. As shown in Fig. S1, the initial state of the device is at high resistance state (HRS) and switches to low resistance state (LRS) at about 1 V during the 1 st set sweep with a compliance current of 0.2 mA. The nonvolatility of the switch is confirmed by the 2nd sweep. However, the devices generally fail to execute the reset process, which means to switch LRS back to HRS, as some of them are only partially reset by applying the 3rd negative sweep and then set to lower resistance at 4th negative sweep (Fig. S2a). Some other devices might be successfully reset to HRS; however, the device subsequently returns to LRS before the negative sweep finishes (Fig. S2b). The failure event for the Ag/h-BN/Cu device as it sets to LRS under negative voltage, which is named as “negative-set”, has also been reported for other resistive switching devices using chemically active bottom electrode materials [37–40]. The negative-set is believed to be resulting from an injection of the

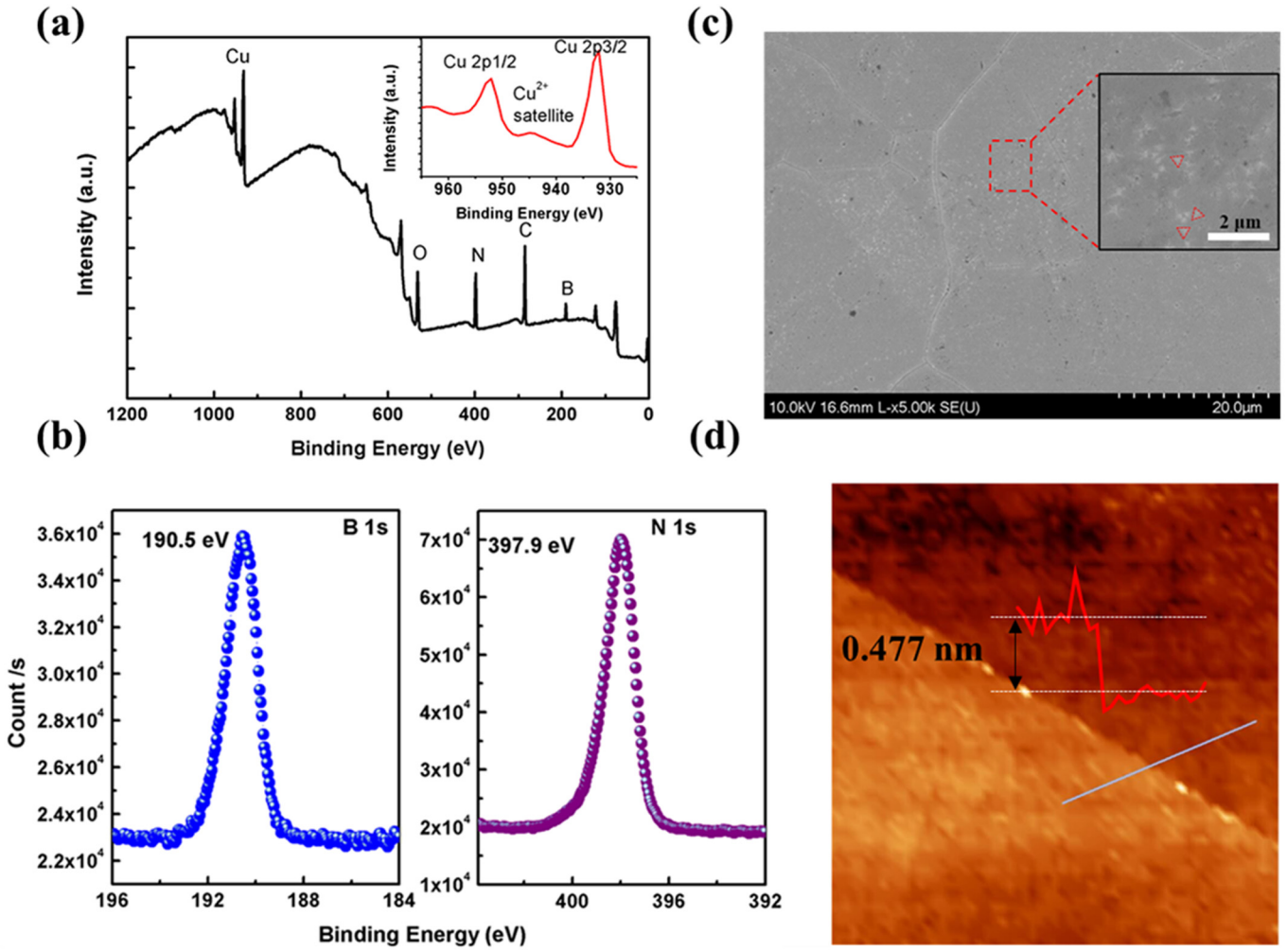

Fig. 1. (a) Survey XPS spectrum of h-BN. Inset: enlarged spectra region of Cu 2p. (b) High-resolution XPS spectra of B 1 s and N 1 s. (c) SEM images of as-grown monolayer h-BN on Cu foil. The inset shows the higher magnification of the dotted square region. (d) AFM images of the transferred h-BN. Inset: the height profile analysis shows an average thickness of ≈0.486 nm, suggesting its monolayer characteristic.

bottom electrode (Cu, in this work) atoms into the switching layer during the negative sweep.

To solve the above problems, we came up with the idea by inserting a thin polymethyl methacrylate (PMMA) inactive layer (~ 10 nm, see Fig. S3) between the top electrode (TE) and h-BN layer (Fig. 2a). The PMMA thin film was chosen as the inserting layer because of its solution-process preparation, low processing temperature, low cost, and high resistivity. Fig. 2b shows the typical I-V curve of an Ag/PMMA/h-BN/Cu memristive device under a compliance current of 1 mA. With such a device structure, the RS properties are greatly improved as both successful set and reset processes can be clearly seen. After the initial forming cycle, the device shows a large on/off ratio ($> 10^3$) and can be stably set from HRS to LRS at about 0.2 V and reset back to HRS at around −0.05 V. The high switching ratio and ultra-low operating voltage of the devices makes a clear contrast to that of many 2D materials-based memristive devices with vertical architectures, in which a large voltage sweep range (> 2 V) is generally required [31,32,41]. Another prominent difference from the Ag/h-BN/Cu structure device is that the resistance of the LRS increases by more than 5 times for devices with the PMMA inserting layer (Fig. 2c, left). The comparison is made under a compliance current of 0.2 mA for both types of devices. In addition, the reset current, defined as the point where the current value starts to decrease during the reset process, is greatly decreased by 2 orders of magnitude for the Ag/PMMA/h-BN/Cu device (Fig. 2c, right). It is also worth noting that the current of Ag/PMMA/BN/Cu during the forming process is slightly larger than that of the Ag/BN/Cu samples (Fig. S4), which is kind of unexpected. A potential explanation for the phenomena is that a small Schottky junction might be formed at the Ag/h-BN interface while Ag/PMMA is always the ohmic contact. On the other hand, the strong dependence of the RS behaviors on TE (Fig. 2d) leads to the resistive switching being governed by the interaction between TE and the monolayer h-BN. Specifically, devices with Ag and Cu TE show similar RS behaviors, although the Cu TE device shows larger set voltages and reset currents. The snapback effect is observed during the set process since our data recording (about 10 milliseconds per data point) cannot catch up with the fast resistance switching process (several nanoseconds according to the report on similar devices [31,32]). In contrast, the Au TE device has a much higher working current (10^{-2}–10^{-1} A) and a small on/off ratio (<10). Apparently, Ag or Cu TE are preferable for constructing the memory device in consideration of the energy efficiency and data robustness. It is worth mentioning that by the transferring process the bottom electrode Cu could also be replaced by more CMOS compatible electrode materials such as TiN thus facilitating the integration into CMOS- fabrication processes.

To clarify the effect of CuO and PMMA layer on RS properties of the device, Ag/PMMA/Cu structure device was fabricated and measured (Fig. S5). The I-V curve shows that by applying a positive sweep, the

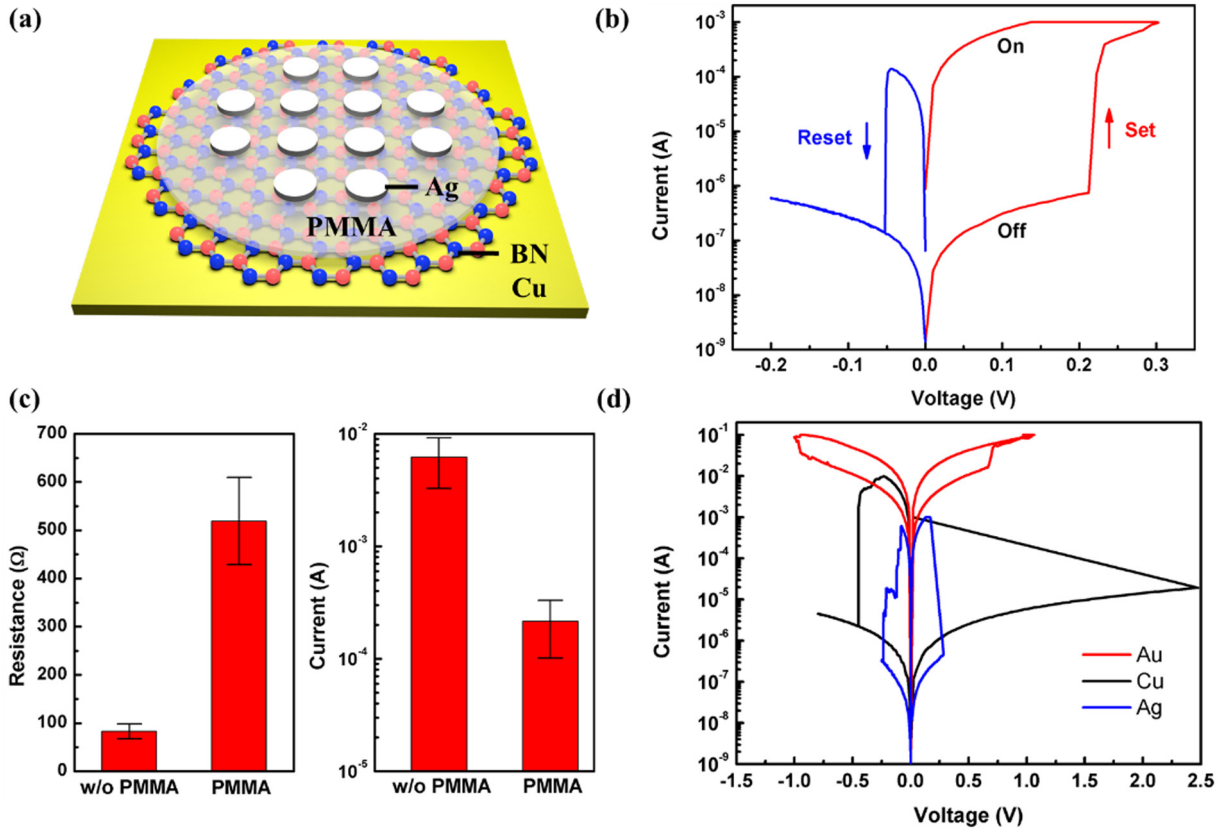

Fig. 2. (a) Schematic of Ag/PMMA/h-BN/Cu devices. (b) Typical I–V cycle of the device. (c) Histogram of five cycles of LRS resistance and reset current for devices with and without PMMA inserting layer. (d) Tailoring the I—V characteristics using different top electrode materials.

current increases abruptly at around 0.4 V, like a set process. However, the negative sweep cannot reset the device. It is possible that the formation of a thermodynamically stable interface between the Ag conduction channel and the PMMA, which can cause irreversible switching. Furthermore, the leakage current of the device is larger than that of the Ag/PMMA/h-BN/Cu device by several orders of magnitude, suggesting the major voltage stress should fall on h-BN. Therefore, it can be concluded that although the existence of CuO and PMMA layer might

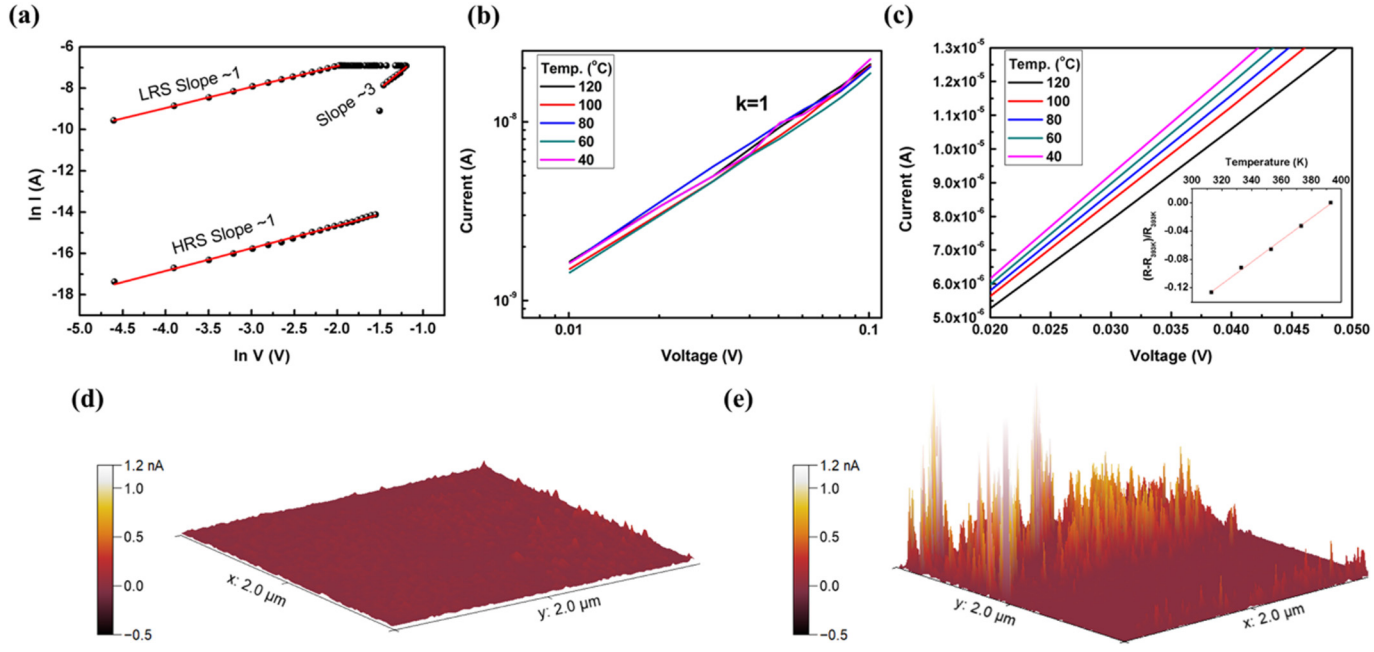

Fig. 3. (a) Ln — ln plot analysis of I — V characteristics of the memory device. (b) Log I–log V curves of the HRS and (c) I—V curves of the LRS at different temperatures. Inset to (c): the $(R - R_{393K})/R_{393K}$ versus T graph. C-AFM images of the Ag/PMMA/h-BN/Cu memory device (d) at the HRS and (e) at the LRS.

influence the forming process, h-BN is the only active layer for RS behaviors of the Ag/PMMA/h-BN/Cu device. In addition, it is worth noting that the compliance current can also greatly influence the RS behaviors of the device. As shown in Fig. S6, the device exhibits threshold switching with a moderate on/off ratio of about 10^2 under a compliance current of 10^{-5} A. The volatile switching phenomena indicate that the memristive effect in Ag/PMMA/h-BN/Cu device may originate from a combination of several processes, such as charge trapping/de-trapping at the film interface [42,43]. However, further study is necessary to understand such behaviors. Although the threshold switching may be of interest for several applications, in this work we focus on the nonvolatile resistive switching phenomenon.

To understand the RS mechanism of the Ag/PMMA/h-BN/Cu memory device, the positive voltage sweeping region of the I-V curve was fitted (Fig. 3a). The fitting result shows that the charge transport behavior at LRS and HRS is linear while during the transition from HRS to LRS the relation can be fitted as $I \propto V^3$, which is the steep current increase region at relatively high voltage [44,45]. The linear fitting relations at both LRS and HRS, however, represent totally different conducting mechanisms. Fig. 3b and c show the temperature-dependent (40–120 °C) log I–log V curves for HRS and LRS obtained with the I_{cc} of 100 μA, respectively. At the HRS, the I—V curves do not show much temperature dependence, as the current exhibits the overlapping linear relationship with the voltage at each temperature, indicating that the tunneling conduction mechanism is plausible to dominate the electron current conduction of the device. At the LRS, however, the temperature-dependent I—V curves for the on-state shown in Fig. 3c suggest that metallic conducting filaments (CFs) are formed. The current decreases with the temperature and has a linear relationship with voltage, confirming the formation of a metallic filament(s) after the set switching process. The calculated temperature coefficient is 1.6×10^{-3} K^{-1}, gained from the $(R - R_{393K})/R_{393K}$ vs. T plot shown in the inset of Fig. 4c. This value is close to those reported temperature coefficients of silver nanoscale filaments (2.5×10^{-3} K^{-1} for defect-free silver nanowires [46] and 1.2×10^{-3} K^{-1} for silver filaments embedded in SiO_x [47]).

To support the filamentary path formation during the RS process, conductive atomic force microscopy (CAFM) was also performed to analyze both the HRS and LRS. A conductive cantilever coated with Pt was used to scan the Ag top electrode of the device. The conductive cantilever was scanned over an area of 2 μm × 2 μm and the read voltage was set to 10 mV. As shown in Fig. 3d, the current value at HRS is very low and no remarkable localized current paths were observed. In contrast, when the memory device is switched to the LRS, several localized current paths emerge, as shown in Fig. 3e, indicating the formation of filamentary conducting channels at LRS.

The resistive switching mechanism can be further supported by the ab-initio simulation results. It is widely reported that boron or nitrogen vacancies commonly exist in h-BN layers [14]. Particularly, boron vacancies are found to be abundant at the grain boundaries [26]. Therefore, the substitute effect of vacancies caused by metal ions was investigated, as shown in Fig. 4a. In the simulation, Ag or Cu ions are firstly placed near the h-BN nanosheet with boron vacancy, and after the structure optimization calculation, the positively charged Ag or Cu ion fills the boron vacancy on the h-BN layer. The optimized structures and electronics of h-BN with 4%, 6.25%, and 11.1% boron atoms replaced by Ag atoms are presented in Fig. 4, and the electronics of pristine single-layer h-BN is also given for reference. The band structure of pristine h-BN exhibits an indirect gap of 4.634 eV (Fig. 4b), which is in good agreement with the previous reference [48,49]. From Fig. 4(c)-(e), it was found that the Ag dopants cause the local deformation of the lattice; however, the main morphology of the lattice is basically maintained. Based on the electronic properties calculation, the metallicity of the monolayer h-BN increases with the increase of replacement percentage. At a relatively low percentage (4%, Fig. 4c), Ag atoms are isolated from each other and thus introduce flat bands, i.e., localized states, in the

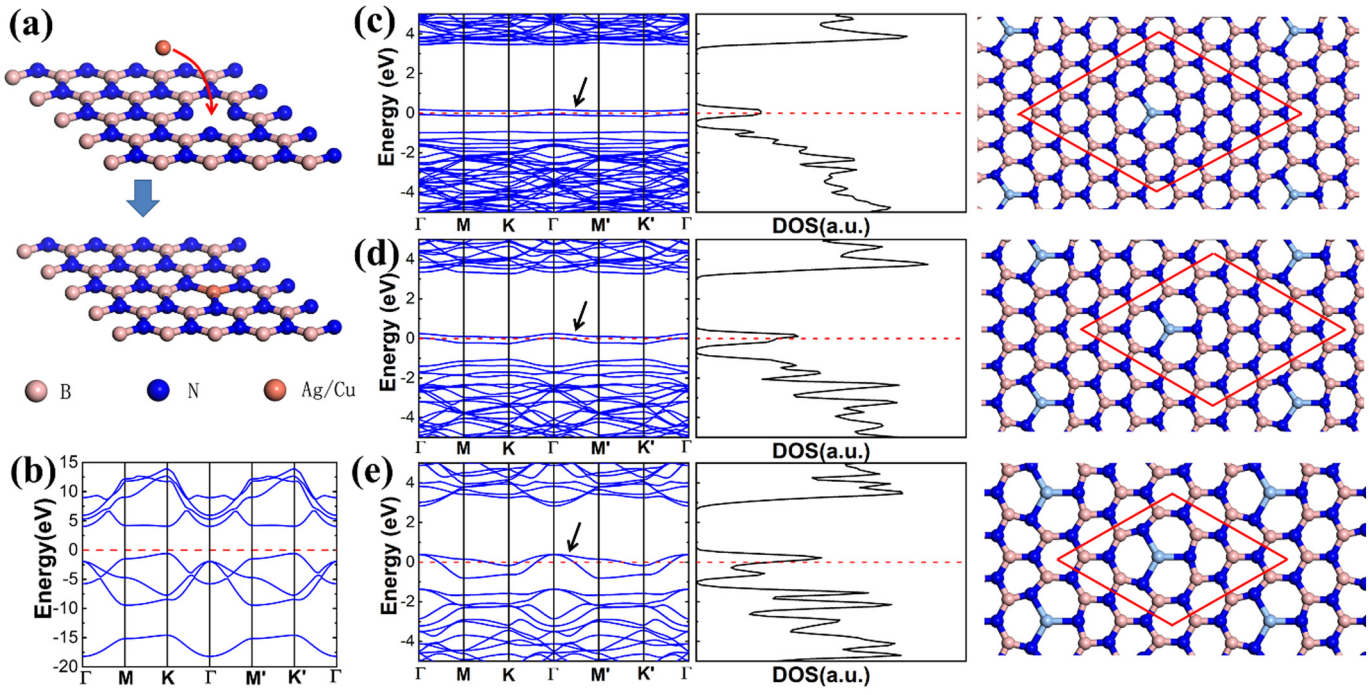

Fig. 4. (a) Schematic illustration for substitute of boron vacancies by metal ions. (b) Band structure of pristine monolayer h-BN. (c) Band structure (left), density of states (middle), and relaxed atomic structure (right) for h-BN with 4% boron atoms replaced by silver atoms. (d, e) The same as (c) but for h-BN with 6.25% and 11.11% boron atoms replaced by Ag atoms. The pink, blue, and light blue spheres represent boron, nitrogen, and silver atoms, respectively. The Fermi level (indicated via dashed lines) has been set to zero for each replacement percentage. The black arrows denote the energy bands originated from silver atoms in the band gap. The supercells of the h-BN sheet are indicated by red parallelograms.

band gap, leading to one DOS peak at Fermi energy level. By increasing the replacement percentage to 6.25% (Fig. 4d), the adjacent Ag atoms begin to interact with each other, and slightly bend the flat bands in the band gap, indicating that the system's metallicity increases. At a high percentage (11.1%, Fig. 4e), the flat bands are bent significantly and cross the Fermi level, leading to partially-filled band feature, therefore the electrons in the partially filled band will be free to move and contribute to the electrical conductivity of the material significantly, resulting in a transition from insulator to metal, as confirmed by the experiment. The ab-initio simulation for Cu ions was also performed and obtained similar results (Fig. S7 and S8). The substitute of metal ions for boron vacancies suggests a local conductive-bridge-like mechanism during the resistive switching in the device.

Therefore, the switching process of the device can be briefly summarized in Fig. 5. In the case of devices without PMMA layer (Fig. 5a), the Ag and Cu ions, which come from TE and BE respectively, are both chemically active and able to fill the boron vacancies. Therefore, it is not easy to achieve a reset procedure for Ag/h-BN/Cu structure device (Fig. S1). Furthermore, the ease of metal substitutions due to the direct contact between TE and h-BN can result in large conducting channels, which mean lower LRS resistance and higher reset current, as shown in Fig. 2c, making the breakdown of CFs more difficult. In contrast, by inserting an interfacial layer between TE and h-BN layer (Fig. 5b), the PMMA not only prevents the overgrowth of the conducting filaments but also helps to block the formation of Cu filaments during the reset process. The conducting filaments in this case can be formed and broken in a more controllable way under the electric field, which improves the device yield and switching reliability.

As a promising candidate for the next-generation solid-state memory due to their distinct advantages in terms of ultimate vertical scaling and low working voltage, the endurance and variation of the Ag/PMMA/h-BN/Cu devices were further verified (Fig. 6a-6d). Different from the previously reported memristive devices based on monolayer materials [31,32], a forming process is generally required for the device, as shown in Fig. 6a. This is reasonable considering that the devices need additional voltage stress to inject Ag through the inserting PMMA layer. The device can be switched stably for at least 100 DC cycles. Further investigation on interface engineering or doping to improve the endurance of the device is needed to meet the requirements for the digital memory. Fig. 6b and c demonstrate the operating voltage and resistance range of the device under the compliance current of 2×10^{-4} A. Importantly, all the operating voltages measured are below 500 mV and the on/off ratio with the read voltage of 20 mV is maintained well above 100, which are sufficiently high for memory application. Note that due to the filamentary nature of the device, it is reasonable to expect an even higher on/off ratio by reducing the device size. Retention of HRS and LRS has been tested and there is no noticeable degradation up to 10^5 s, indicating its nonvolatile nature. Moreover, the subnanometer

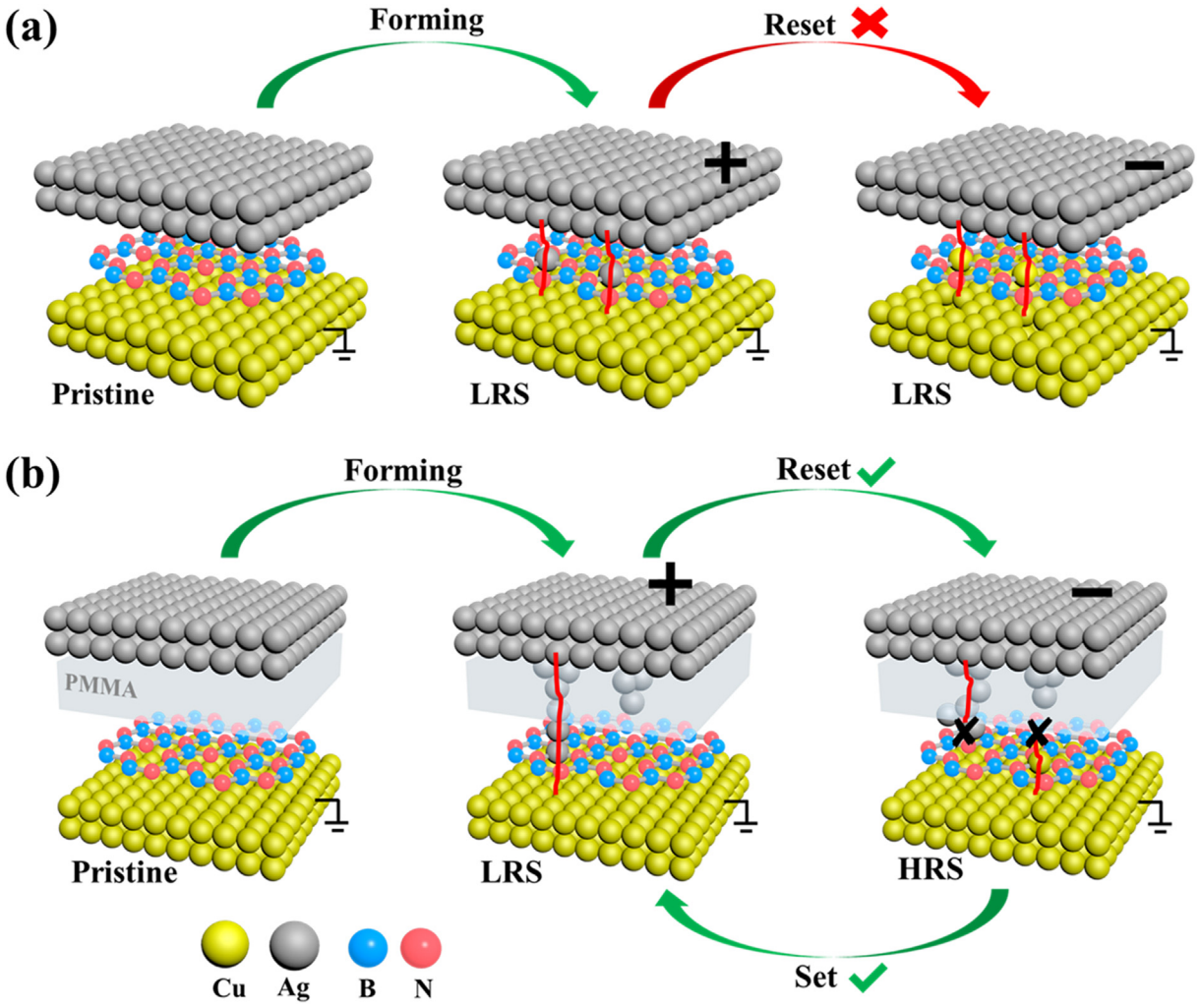

Fig. 5. Schematic of the resistive switching process for (a) Ag/h-BN/Cu and (b) Ag/PMMA/h-BN/Cu devices, respectively. Without the PMMA inserting layer, the active Ag and Cu ions might easily enter the h-BN monolayer, making the device hard to reset to HRS; In contrast, the PMMA interfacial layer can help to block the conducting filament formation during the reset process and thus obtain a more reliable device.

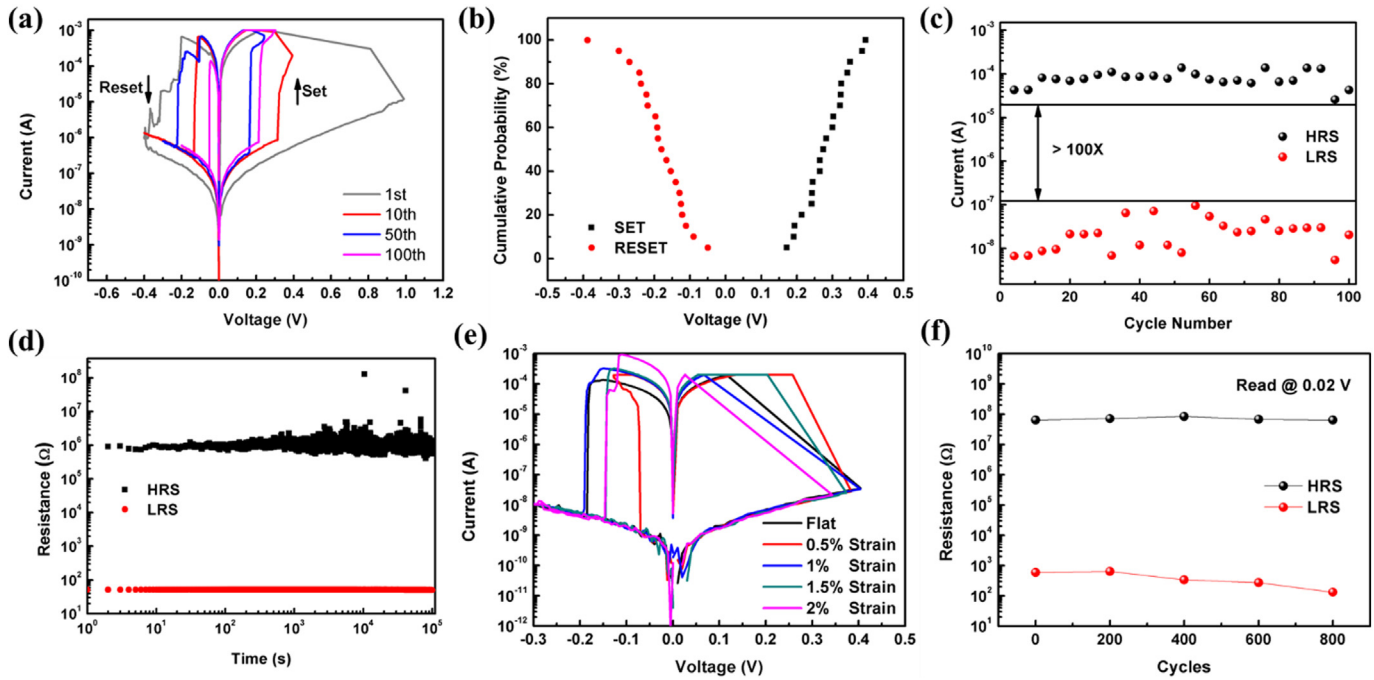

Fig. 6. (a) Resistive switching characteristics of the h-BN device with 100 cycles, the compliance current is 1 mA. (b,c) switching voltage and endurance distribution of the h-BN device with 100 manual DC switching cycles. (d) Time-dependent measurements of the h-BN device featuring stable retention at room temperature. The resistance of the HRS and LRS is extracted by monitoring the current at a small bias of 20 mV. (e) Stable switching behaviors under gradual bending conditions. (f) Resistance distribution with 800 bending cycles at 1% strain.

thinness and high breaking strain of the monolayer h-BN make the device highly desirable for flexible nonvolatile memory. Fig. 6e shows the I-V curves under the I_{cc} of 200 μA while the device is holding by a 15 × 15 mm^2 PET substrate, which is bent from flat to a certain radius of curvature. The memory device is perfectly functional under up to 2% strain. The endurance to mechanical bending cycles was also examined. The memory device exhibits a stable on/off ratio (>10^5) distribution without any significant electrical degradation during 800 bending cycles (Fig. 6f). The resistive switching characteristics of representative reported devices based on 2D materials are summarized in Table S1. The device shows a comparable ON/OFF ratio, long retention time and good flexibility. Importantly, the device shows ultra-low working voltage, which might be useful for unconventional applications such as mobile computing or medical devices, using a person's body temperature or exercise to meet their electricity needs due to the low power consumption.

4. Conclusion

In summary, a transfer and lithography-free resistive switching device based on monolayer h-BN with a vertical metal-insulator-metal structure was reported. By inserting a thin PMMA interfacial layer between h-BN and TE, the device shows stable bipolar resistive switching behavior with a large on/off ratio (up to 10^5), low operating voltage (< 500 mV), and good flexibility. From conduction mechanism analysis by temperature-dependent electron transport studies and C-AFM measurements, it is demonstrated that tunneling conduction was shown in HRS and LRS current conducts via metallic CFs, which are formed by the substitute of metal ions for lattice vacancies in h-BN and proven by ab-initio simulations. We highlight that the polymer interfacial layer plays a critical role to achieve reliable resistive switching behavior by reducing the CF overgrowth and blocking the excess CFs formation from the bottom Cu foil. Although the endurance and switching uniformity of the devices are not yet sufficient to meet the critical requirements for digital memory and will be the focus of a future report, this work illustrates a scalable interface engineering method to enhance the performance of ReRAM devices based on monolayer 2D materials.

Notes

The authors declare no competing financial interest.

Declaration of Competing Interest

The authors declare that they have no known competing financial interests or personal relationships that could have appeared to influence the work reported in this paper.

Acknowledgments

The authors acknowledge the financial support from the National Natural Science Foundation of China (11847059, 61604045, 51872054, 12004083), the Natural Science Foundation of Guangdong Province (2018A030313041), the Department of Education of Guangdong Province (2018KZDXM052) and the National Supercomputer Center in Guangzhou.

Appendix A. Supplementary data

Supplementary data to this article can be found online at https://doi.org/10.1016/j.matdes.2020.109366.

References

[1] Q.H. Wang, K. Kalantar-Zadeh, A. Kis, J.N. Coleman, M.S. Strano, Electronics and optoelectronics of two-dimensional transition metal dichalcogenides, Nat Nano 7 (11) (2012) 699–712.
[2] K. Kang, S. Xie, L. Huang, Y. Han, P.Y. Huang, K.F. Mak, C.-J. Kim, D. Muller, J. Park, High-mobility three-atom-thick semiconducting films with wafer-scale homogeneity, Nature 520 (7549) (2015) 656–660.

[3] J. Tao, J. Chai, X. Lu, L.M. Wong, T.I. Wong, J. Pan, Q. Xiong, D. Chi, S. Wang, Growth of wafer-scale MoS2 monolayer by magnetron sputtering, Nanoscale 7 (6) (2015) 2497–2503.
[4] L. Tan, N. Li, S. Chen, Z.-Q. Liu, Self-assembly synthesis of CuSe@graphene-carbon nanotubes as efficient and robust oxygen reduction electrocatalysts for microbial fuel cells, J. Mater. Chem. A 4 (31) (2016) 12273–12280.
[5] Y. Huang, Z. Yang, A. Liu, J. Fu, Nonlinear Buckling Analysis of Functionally Graded Graphene Reinforced Composite Shallow Arches with Elastic Rotational Constraints under Uniform Radial Load, MATERIALS 11 (6) (2018).
[6] Z. Song, W. Li, Y. Bao, W. Wang, Z. Liu, Bioinspired Microstructured Pressure Sensor Based on a Janus Graphene Film for Monitoring Vital Signs and Cardiovascular Assessment, ADVANCED ELECTRONIC MATERIALS 4 (11) (2018).
[7] N. Li, K.-X. Guo, S. Shao, G.-H. Liu, Polaron effects on the optical absorption coefficients and refractive index changes in a two-dimensional quantum pseudodot system, Opt. Mater. 34 (8) (2012) 1459–1463.
[8] J. Dong, Z. Qiao, Y. Pan, S.B. Peh, Y.D. Yuan, Encapsulation and protection of ultrathin two-dimensional porous organic Nanosheets within biocompatible metal-organic frameworks for live-cell imaging, Chem. Mater. 31 (13) (2019) 4897–4912.
[9] D. Wang, H. Li, L. Zhang, Z. Sun, D. Han, First-principles study on OH-functionalized 2D electrides: Ca2NOH and Y2C(OH)(2)promising two-dimensional monolayers for metal-ion batteries, Appl Surf Sci 478 (2019) 459–464.
[10] X. Zhou, J. Jia, Z. Luo, G. Su, T. Yue, Remote induction of cell autophagy by 2D MoS2 Nanosheets via perturbing cell surface receptors and mTOR pathway from outside of cells, ACS Appl. Mater. Interfaces 11 (7) (2019) 6829–6839.
[11] C. Peng, P. Wei, X. Chen, Y. Zhang, F. Zhu, A hydrothermal etching route to synthesis of 2D MXene (Ti3C2, Nb2C): enhanced exfoliation and improved adsorption performance, Ceram. Int. 44 (15) (2018) 18886–18893.
[12] C. Peng, P. Wei, X. Li, Y. Liu, Y. Cao, High efficiency photocatalytic hydrogen production over ternary Cu/TiO2@Ti3C2Tx enabled by low-work-function 2D titanium carbide, NANO ENERGY 53 (2018) 97–107.
[13] J. Chen, X. Wang, X. Yu, L. Yao, Z. Duan, High dielectric constant and low dielectric loss poly(vinylidene fluoride) nanocomposites via a small loading of two-dimensional Bi2Te3@Al2O3 hexagonal nanoplates, J. Mater. Chem. C 6 (2) (2018) 271–279.
[14] C. Tan, Z. Liu, W. Huang, H. Zhang, Non-volatile resistive memory devices based on solution-processed ultrathin two-dimensional nanomaterials, Chem. Soc. Rev. 44 (9) (2015) 2615–2628.
[15] Z. Rao, W. Liang, H. Huang, J. Ge, W. Wang, S. Pan, High sensitivity and rapid response ultraviolet photodetector of a tetragonal CsPbCl3 perovskite single crystal, Opt. Mater. Express 10 (6) (2020) 1374–1382.
[16] V. Prusakova, C. Collini, L. Lunelli, L. Vanzetti, A. Chiappini, L. Lorenzelli, C. Pederzolli, A. Chiasera, M. Ferrari, S. Dirè, Towards low voltage resistive switch in sol-gel derived TiO2/Ta2O5 stack thin films, Mater Design 105 (2016) 359–365.
[17] W. Hu, L. Zou, X. Lin, C. Gao, Y. Guo, D. Bao, Unipolar resistive switching effect and mechanism of solution-processed spinel Co3O4 thin films, Mater Design 103 (2016) 230–235.
[18] A.C. Khot, N.D. Desai, K.V. Khot, M.M. Salunkhe, M.A. Chougule, T.M. Bhave, R.K. Kamat, K.P. Musselman, T.D. Dongale, Bipolar resistive switching and memristive properties of hydrothermally synthesized TiO2 nanorod array: effect of growth temperature, Mater Design 151 (2018) 37–47.
[19] Z. Chen, Y. Yu, L. Jin, Y. Li, Q. Li, T. Li, Y. Zhang, H. Dai, J. Yao, Artificial synapses with photoelectric plasticity and memory behaviors based on charge trapping memristive system, Mater Design 188 (2020) 108415.
[20] W. Lv, H. Wang, L. Jia, X. Tang, C. Lin, L. Yuwen, L. Wang, W. Huang, R. Chen, Tunable nonvolatile memory behaviors of PCBM-MoS2 2D nanocomposites through surface deposition ratio control, ACS Appl. Mater. Interfaces 10 (7) (2018) 6552–6559.
[21] J. Liu, Z. Zeng, X. Cao, G. Lu, L.H. Wang, Q.L. Fan, W. Huang, H. Zhang, Preparation of MoS(2)-polyvinylpyrrolidone nanocomposites for flexible nonvolatile rewritable memory devices with reduced graphene oxide electrodes, Small 8 (22) (2012) 3517–3522.
[22] V.K. Sangwan, D. Jariwala, I.S. Kim, K.S. Chen, T.J. Marks, L.J. Lauhon, M.C. Hersam, Gate-tunable memristive phenomena mediated by grain boundaries in single-layer MoS2, Nat. Nanotechnol. 10 (5) (2015) 403–406.
[23] V.K. Sangwan, H.S. Lee, H. Bergeron, I. Balla, M.E. Beck, K.S. Chen, M.C. Hersam, Multi-terminal memtransistors from polycrystalline monolayer molybdenum disulfide, Nature 554 (7693) (2018) 500–504.
[24] D. Li, B. Wu, X. Zhu, J. Wang, B. Ryu, W.D. Lu, W. Lu, X. Liang, MoS2 Memristors exhibiting variable switching characteristics toward biorealistic synaptic emulation, ACS Nano 12 (9) (2018) 9240–9252.
[25] R. Xu, H. Jang, M.H. Lee, D. Amanov, Y. Cho, H. Kim, S. Park, H.J. Shin, D. Ham, Vertical MoS2 double-layer Memristor with electrochemical metallization as an atomic-scale synapse with switching thresholds approaching 100 mV, Nano Lett. 19 (4) (2019) 2411–2417.
[26] C. Pan, Y. Ji, N. Xiao, F. Hui, K. Tang, Y. Guo, X. Xie, F.M. Puglisi, L. Larcher, E. Miranda, L. Jiang, Y. Shi, I. Valov, P.C. McIntyre, R. Waser, M. Lanza, Coexistence of grain-boundaries-assisted bipolar and threshold resistive switching in multilayer hexagonal boron nitride, Adv. Funct. Mater. 27 (10) (2017) 1604811.
[27] Y. Shi, X. Liang, B. Yuan, V. Chen, H. Li, F. Hui, Z. Yu, F. Yuan, E. Pop, H.S.P. Wong, M. Lanza, Electronic synapses made of layered two-dimensional materials, Nature Electronics 1 (8) (2018) 458–465.
[28] M. Wang, S. Cai, C. Pan, C. Wang, X. Lian, Y. Zhuo, K. Xu, T. Cao, X. Pan, B. Wang, S.-J. Liang, J.J. Yang, P. Wang, F. Miao, Robust memristors based on layered two-dimensional materials, Nature Electronics 1 (2) (2018) 130–136.
[29] M. Kim, R. Ge, X. Wu, X. Lan, J. Tice, J.C. Lee, D. Akinwande, Zero-static power radio-frequency switches based on MoS2 atomristors, Nat. Commun. 9 (1) (2018) 2524.
[30] M. Kim, E. Pallecchi, R. Ge, X. Wu, G. Ducournau, J.C. Lee, H. Happy, D. Akinwande, Analogue switches made from boron nitride monolayers for application in 5G and terahertz communication systems, Nature Electronics 3 (2020) 479–485.
[31] X. Wu, R. Ge, P.A. Chen, H. Chou, Z. Zhang, Y. Zhang, S. Banerjee, M.H. Chiang, J.C. Lee, D. Akinwande, Thinnest nonvolatile memory based on monolayer h-BN, Adv. Mater. 31 (15) (2019), e1806790, .
[32] R. Ge, X. Wu, M. Kim, J. Shi, S. Sonde, L. Tao, Y. Zhang, J.C. Lee, D. Akinwande, Atomristor: Nonvolatile Resistance Switching in Atomic Sheets of Transition Metal Dichalcogenides, Nano Lett 18 (1) (2018) 434–441.
[33] C. Tan, H. Zhang, Two-dimensional transition metal dichalcogenide nanosheet-based composites, Chem. Soc. Rev. 44 (9) (2015) 2713–2731.
[34] K. Zhu, X. Liang, B. Yuan, M.A. Villena, C. Wen, T. Wang, S. Chen, F. Hui, Y. Shi, M. Lanza, Graphene-boron nitride-graphene cross-point Memristors with three stable resistive states, ACS Appl. Mater. Interfaces 11 (41) (2019) 37999–38005.
[35] L. Li, C. Hu, L. Zhang, G. Yu, L. Lyu, Framework cu-doped boron nitride nanobelts with enhanced internal electric field for effective Fenton-like removal of organic pollutants, J. Mater. Chem. A 7 (12) (2019) 6946–6956.
[36] K.K. Kim, A. Hsu, X. Jia, S.M. Kim, Y. Shi, M. Hofmann, D. Nezich, J.F. Rodriguez-Nieva, M. Dresselhaus, T. Palacios, J. Kong, Synthesis of monolayer hexagonal boron nitride on cu foil using chemical vapor deposition, Nano Lett. 12 (1) (2012) 161–166.
[37] S. Balatti, S. Ambrogio, Z. Wang, S. Sills, A. Calderoni, N. Ramaswamy, D. Ielmini, Voltage-controlled cycling endurance of HfOx-based resistive-switching memory, IEEE T Electron Dev 62 (10) (2015) 3365–3372.
[38] Z. Wang, S. Ambrogio, S. Balatti, S. Sills, A. Calderoni, N. Ramaswamy, D. Ielmini, Postcycling degradation in metal-oxide bipolar resistive switching memory, IEEE T Electron Dev 63 (11) (2016) 4279–4287.
[39] S. Pan, Z. Liu, W. Lu, Synthesis of naked plasmonic/magnetic au/Fe3O4 nanostructures by plasmon-driven anti-replacement reaction, Nanotechnology 30 (6) (2018), 065605, .
[40] S. Pan, X. Zhang, W. Lu, S.F. Yu, Plasmon-engineered anti-replacement synthesis of naked cu nanoclusters with ultrahigh electrocatalytic activity, J. Mater. Chem. A 6 (38) (2018) 18687–18693.
[41] L. Zhang, T. Gong, H. Wang, Z. Guo, H. Zhang, Memristive devices based on emerging two-dimensional materials beyond graphene, Nanoscale 11 (26) (2019) 12413–12435.
[42] M. Kumar, S. Abbas, J. Kim, All-oxide-based highly transparent photonic synapse for neuromorphic computing, ACS Appl. Mater. Interfaces 10 (40) (2018) 34370–34376.
[43] Y. Kim, Y.J. Kwon, D.E. Kwon, K.J. Yoon, J.H. Yoon, S. Yoo, H.J. Kim, T.H. Park, J.-W. Han, K.M. Kim, C.S. Hwang, Nociceptive Memristor, Adv. Mater. 30 (2018) 1704320.
[44] Y.C. Yang, F. Pan, Q. Liu, M. Liu, F. Zeng, Fully room-temperature-fabricated nonvolatile resistive memory for ultrafast and high-density memory application, Nano Lett. 9 (4) (2009) 1636–1643.
[45] X. Yan, J. Zhao, S. Liu, Z. Zhou, Q. Liu, J. Chen, X.Y. Liu, Memristor with ag-cluster-doped TiO2 films as artificial synapse for Neuroinspired computing, Adv. Funct. Mater. 1705320 (2017).
[46] A. Bid, A. Bora, A.K. Raychaudhuri, Temperature dependence of the resistance of metallic nanowires of diameter >15 nm: applicability of Bloch-Grüneisen theorem, Phys. Rev. B 74 (3) (2006), 035426, .
[47] J.H. Yoon, Z. Wang, K.M. Kim, H. Wu, V. Ravichandran, Q. Xia, C.S. Hwang, J.J. Yang, An artificial nociceptor based on a diffusive memristor, Nat. Commun. 9 (1) (2018) 417.
[48] R.M. Ribeiro, N.M.R. Peres, Stability of boron nitride bilayers: ground-state energies, interlayer distances, and tight-binding description, Phys. Rev. B 83 (23) (2011) 235312.
[49] N. Pantha, P. Bissokarma, N.P. Adhikari, First-principles study of electronic and magnetic properties of nickel doped hexagonal boron nitride (h-BN), The European Physical Journal B 93 (9) (2020) 164.